Wide-area scanner for high-sp microscopy

doi: 10.1063/1.4803449

Wide-area scanner for high-speed atomic force microscopy

Hiroki Watanabe,[1] Takayuki Uchihashi,[1,2] Toshihide Kobashi,[1] Mikihiro Shibata,[3] Jun Nishiyama,[3] Ryohei Yasuda,[3,4] and Toshio Ando[1,2,a)]

[1]*Department of Physics, College of Science and Engineering, Kanazawa University, Kanazawa 920-1192, Japan*
[2]*Bio-AFM Frontier Research Center, College of Science and Engineering, Kanazawa University, Kanazawa 920-1192, Japan*
[3]*Department of Neurobiology, Duke University Medical Center, Durham, North Carolina 27710, USA*
[4]*Max Planck Florida Institute, Jupiter, Florida 33458, USA*

(Received 25 February 2013; accepted 11 April 2013; published online 3 May 2013)

High-speed atomic force microscopy (HS-AFM) has recently been established. The dynamic processes and structural dynamics of protein molecules in action have been successfully visualized using HS-AFM. However, its maximum scan ranges in the X- and Y-directions have been limited to ~1 μm and ~4 μm, respectively, making it infeasible to observe the dynamics of much larger samples, including live cells. Here, we develop a wide-area scanner with a maximum XY scan range of ~46 × 46 μm^2 by magnifying the displacements of stack piezoelectric actuators using a leverage mechanism. Mechanical vibrations produced by fast displacement of the X-scanner are suppressed by a combination of feed-forward inverse compensation and the use of triangular scan signals with rounded vertices. As a result, the scan speed in the X-direction reaches 6.3 mm/s even for a scan size as large as ~40 μm. The nonlinearity of the X- and Y-piezoelectric actuators' displacements that arises from their hysteresis is eliminated by polynomial-approximation-based open-loop control. The interference between the X- and Y-scanners is also eliminated by the same technique. The usefulness of this wide-area scanner is demonstrated by video imaging of dynamic processes in live bacterial and eukaryotic cells. © *2013 AIP Publishing LLC*. [http://dx.doi.org/10.1063/1.4803449]

I. INTRODUCTION

Over the last two decades, various efforts have been made to increase the imaging rate of atomic force microscopy (AFM).[1–4] The bandwidth of feedback control that maintains the tip–sample interaction force constant has been increased to ~100 kHz, enabling the capture of protein molecules on video at sub-100-ms temporal and sub-molecular spatial resolution. Importantly, the tip–sample interaction does not disturb the function of fragile proteins and weak protein–protein interactions.[4] High-speed AFM (HS-AFM) is now started to be routinely used to study the dynamic processes of purified protein molecules under physiological conditions.[5] For example, dynamic conformational changes of motor and membrane proteins at work,[6–10] dynamic protein–protein interactions,[11–14] dynamics occurring in 2D protein crystals,[15] and wiggling motion of intrinsically disordered proteins[16] have been successfully visualized. However, to achieve this high-speed, low-invasive performance, the scan range has had to be limited to approximately 1 μm, 4 μm, and 1 μm in the X-, Y-, and Z-directions (at 100 V), respectively. This is because a smaller maximum displacement allows us to build a compact scanner, and hence attain higher resonant frequencies and scan speeds.

The limited scan ranges are sufficient for imaging protein molecules in action. However, in the biological sciences, there is also an increasing demand that dynamic events occurring in live cells be directly visualized at high spatiotemporal resolution. Toward meeting this demand, wide-area scanners with scan ranges of >10 × 10 μm^2 have been developed for HS-AFM.[17–21] Their excellent performance has largely been demonstrated by fast imaging of hard material surfaces. However, fast wide-area imaging is difficult for soft biological samples. Fantner *et al.*[20] recently performed fast wide-area imaging of bacterial cells to study the effect of antimicrobial peptides on the surface of *E. coli* cells. The imaging rates used there are 12.8 s/frame (scan rate, 20 lines/s; scan speed, 0.12 mm/s) for an area of 3 × 3 μm^2 and 128 s/frame (scan rate, 2 lines/s; scan speed, 0.036 mm/s) for an area of 9 × 3 μm^2. Thus, despite these previous advances, AFM's capability for faster and wider bioimaging remains to be pursued.

To achieve this capability, we need techniques for magnifying the displacement of a piezoelectric actuator, damping mechanical vibrations, expanding the frequency bandwidth, minimizing the nonlinear displacement, and minimizing the interference between the X- and Y-displacements. In addition, we need a Z-scanner with a large maximum displacement as well as a high feedback bandwidth. In this study, we developed these techniques. For a hard material surface, the techniques achieve an imaging rate of 3 s/frame (scan rate, 85 lines/s) for a 40 × 40 μm^2 area. This rate corresponds to a scan speed of 6.8 mm/s, which is faster than the previous fastest record.[19]

To demonstrate the capability and usefulness of this new wide-area scanner in bioimaging, we observed the bacteriolysis process of *Bacillus* (*B.*) *subtilis* subjected to lysozyme and the dynamic processes of actin retrograde flow and

a)Author to whom correspondence should be addressed. Electronic mail: tando@staff.kanazawa-u.ac.jp.

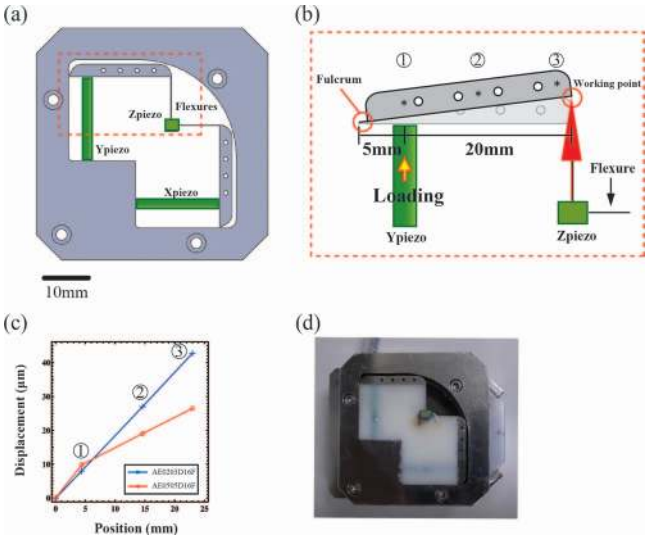

FIG. 1. (a) Scheme of newly designed wide-area scanner for high-speed AFM. (b) Enlarged view of the leverage-based displacement magnification mechanism. Asterisks indicate the points that are 5 mm (1), 15 mm (2), and 23 mm (3) distant from the fulcrum. Displacements were measured at these points. (c) Displacements caused by the extension of two different piezoactuators (Piezo-1, blue line; Piezo-2, red line) measured at three different points along the lever indicated in (b). (d) Photograph of the wide-area scanner.

endocytosis in HeLa cells. Even for an area as wide as $20 \times 20\ \mu m^2$, *B. subtilis* cells were successfully imaged at 15 s/frame (scan rate, 13.3 lines/s; scan speed, 0.53 mm/s) with 200×200 pixels. We also showed that this wide-area scanner can be used to image proteins in a narrow area with an imaging rate comparable to that achieved by our fast small-area scanner.

II. MECHANICAL DESIGN OF WIDE-AREA SCANNER

To achieve large displacements in the X- and Y-directions, we magnified the displacements of the X- and Y-piezoactuators using the third-class leverage mechanism. Figure 1(a) shows a schematic of the scanner designed in this study. The entire frame mechanism made of aluminum (A5052) was obtained by monolithic fabrication. The X- and Y-piezoactuators are arranged symmetrically with respect to the supporting base to which the Z-piezoactuator is attached. This symmetrical configuration enables us to choose either the X- or Y-direction as the fast scanning direction and rotate the scan direction.[22]

The leverage mechanism employed is shown schematically in Fig. 1(b). The entire lever length is 25 mm, and the point of effort to which the piezoactuator is glued is 5 mm distant from the fulcrum; i.e., the designed lever ratio is 5. We tested two different types of piezoactuators: piezo-I (AE0203D16F, Tokin-NEC) with dimensions of $2 \times 3 \times 20\ mm^3$, a nominal unloaded displacement of 11.6 μm at 100 V, and a resonant frequency of 69 kHz, and piezo-II (AE0505D16F, Tokin-NEC) with dimensions of $5 \times 5 \times 20\ mm^3$ and the same nominal unloaded displacement and resonant frequency as piezo I. Because piezo-II can generate a higher force (850 N) than piezo-I (200 N), the magnified displacement by piezo-II under a loaded condition was expected to be larger than that by piezo-I. However, this was not the case. Figure 1(c) shows the displacements of the lever at three different points along the lever [indicated in Fig. 1(b)] that were caused by piezo-I (blue line) and piezo-II (red line) when 100 V was applied. At point 1, 5 mm distant from the fulcrum, the displacement caused by piezo-II was slightly larger than that caused by piezo-I. However, at points 2 and 3, 15 mm and 23 mm distant from the fulcrum, respectively, the displacements by piezo-I were larger than those by piezo II. This is because piezo II is glued to the lever over a wider area; the wider glued area results in a nonlinear displacement of the lever. Thus, we chose piezo-I for the X- and Y-scanners and achieved maximum scan ranges of 46.7 μm for the X-direction and 45.7 μm for the Y-direction. These measured values were ~20% smaller than the displacement of 58 μm calculated from the lever ratio and the unloaded displacement of piezo-I at 100 V.

A photograph of the fully assembled scanner is shown in Fig. 1(d). The gap spaces in the scanner were filled with an elastomer consisting of polyurethane (EXSEAL Co., sponge hardness = 5: similar softness to skin of face or arms). This filling with the elastomer passively damps low-frequency vibrations of the scanner.

III. IMPROVEMENT OF SCANNER PERFORMANCE

A. Vibration damping for X-scan

Ideally, the trajectory of an X-scan is an isosceles triangle as a function of time. However, when the X-scanner is driven by a voltage that changes in the form of an isosceles triangle wave, high harmonic frequency components contained in the vertices of the triangular wave excite the X-scanner, resulting in the generation of vibrations at its resonant frequencies. Any X-scanners for wider-area scanning generally have lower resonant frequencies and therefore are apt to vibrate when scanned quickly. Figure 2(a) shows the frequency response of the wide-area X-scanner built as described above (red line, amplitude; blue line, phase). Here, the lateral displacement was measured using a laser displacement meter at the central base to which the Z-piezoactuator is attached. Figure 2(b) shows an input triangular wave (black line) of 28 Hz and the measured displacement (red line). This frequency corresponds to an imaging rate of 9 s/frame for a 256×256 pixel image. At this scan speed, vibrations are not excited even around the vertices of the triangular wave because higher harmonic components contained in the triangular wave are negligible around the resonant frequency of the X-scanner (~2 kHz). In contrast, during a scan at 85 Hz, vibrations of 2 kHz appeared, as shown by the red line in Fig. 2(c).

In practice, non-negligible vibrations are produced when the fundamental frequency of the input triangular wave is higher than ~2% of the first resonant frequency of the X-scanner. To overcome this adverse effect, modified lateral scan waves, such as sinusoidal,[19] spiral,[23] cycloid,[24] and Lissajous[25] waves have been proposed. Sinusoidal scanning is the simplest solution, but both the left and right end areas of an image are greatly distorted. Assuming that an approximately linear scan is obtained when the scan velocity is higher

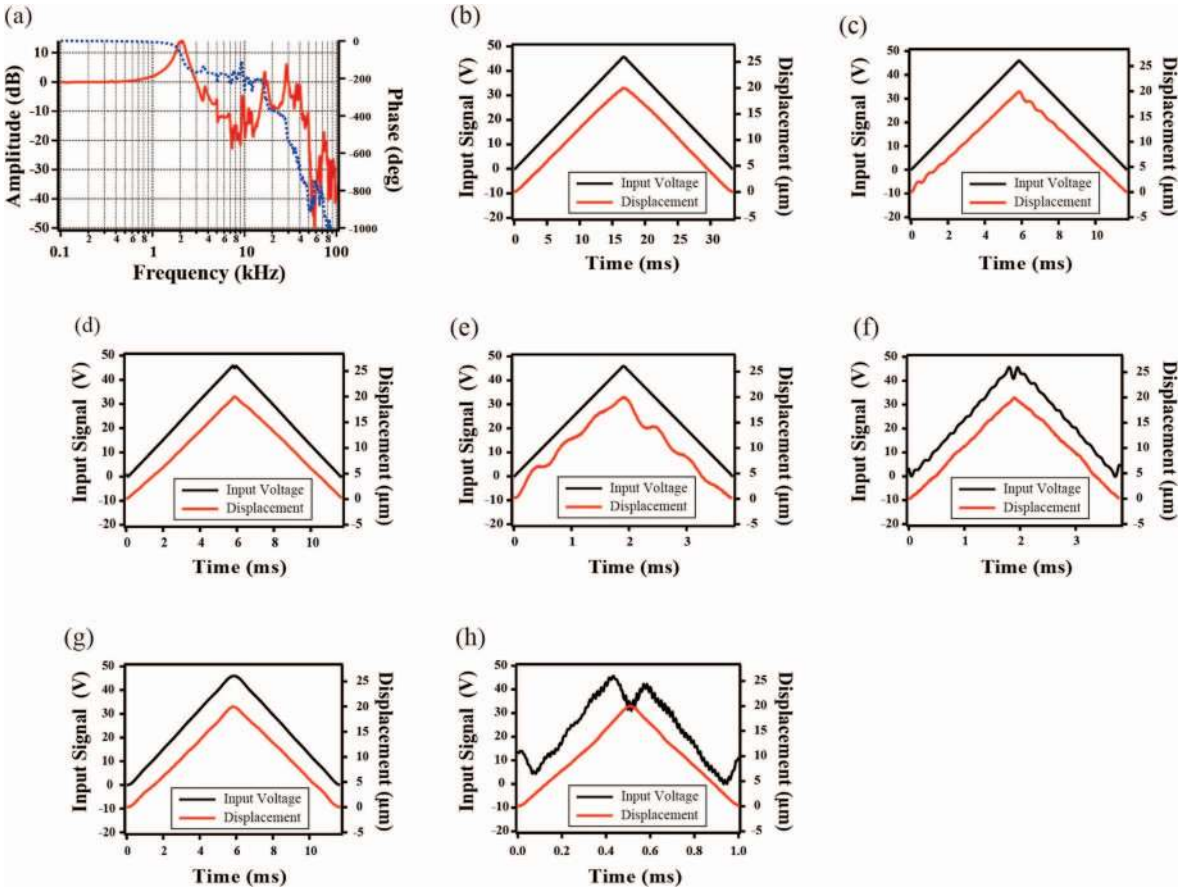

FIG. 2. Effects of vibration damping on displacement of X-scanner. (a) Frequency spectra of mechanical response of the X-scanner (red line, amplitude; blue line, phase). (b) Driving signal of 28 Hz with a non-modified triangular wave form (black line) and corresponding displacement (red line). (c) Driving signal of 85 Hz with a non-modified triangular wave form (black line) and corresponding displacement (red line). (d) Driving signal of 85 Hz with a triangular wave form modified by inverse compensation (black line) and corresponding displacement (red line). (e) Driving signal of 256 Hz with a non-modified triangular wave (black line) and corresponding displacement (red line). (f) Driving signal of 256 Hz with a triangular wave form modified by the inversed compensation (black line) and corresponding displacement (red line). (g) Driving signal of 85 Hz with a rounded triangular wave form containing harmonics up to the ninth order (black line) and corresponding displacement. (h) Driving signal of 1 kHz obtained after modification by inverse compensation of a rounded triangular wave form containing harmonics up to the ninth order (black line) and corresponding displacement (red line).

than 85% of the maximum velocity, the nonlinear scan area is 65% of the full image. Moreover, the resolution in the less-distorted central image area is low (i.e., a smaller number of pixels). Even after linearization of the obtained image by calculation, the lower resolution in the most important central image area cannot be changed. Although the spiral, cycloid, and Lissajous waves contain no higher harmonic frequencies, the procedures for producing the scan signals, reconstructing the image, and compensating for the hysteresis effects of the piezoactuators are complicated. Moreover, the cantilever tends to be twisted by a lateral dragging force component perpendicular to the lever arm, which hampers the sample height measurement. Here, we employed two approaches to the elimination of X-scanner vibrations: an inversion-based feed-forward damping[17,26] and a modified triangular wave with reduced higher harmonics.[27,28]

The black line in Fig. 2(d) shows the modified triangular wave obtained after filtration of a triangular wave through an inverse transfer function that was constructed using the frequency response shown in Fig. 2(a). Here, the triangular wave to be filtered was constructed with the first 20 terms in the Fourier cosine series of an isosceles triangle function. The vibrations previously observed [Fig. 2(c)] disappeared to a practical extent with this method [the red line in Fig. 2(d)]. Even during scanning at a higher frequency of 256 Hz (corresponding to a imaging rate of 1 s/frame for 256 lines), vibrations were suppressed significantly (but not to a practical extent) by this damping, as shown by the red line in Fig. 2(f), compared with the result observed without damping [the red line in Fig. 2(e)]. In principle, this damping method can significantly extend the bandwidth of the X-scanner, but in reality, the limited gain and current of a piezodriver at high frequencies limit the bandwidth extension. Moreover, the frequency response of the X-scanner occasionally varies to some extent depending on the sample attached. Therefore, for scan frequencies higher than ∼100 Hz, vibration damping to a practical extent cannot be achieved by this method alone.

Another damping method we tested was simple rounding of the vertices of the triangular wave.[27] An isosceles triangular wave is composed of a cosine wave with the fundamental frequency and an infinite series of its odd higher harmonics.

By reducing the number of higher harmonics, one can easily generate a triangular wave with round vertices. As shown in Fig. 2(a), the amplitude gain of the X-scanner starts to increase at 500 Hz. Assuming that the gain tolerance is less than 1 dB, the highest frequency of harmonics to be included in the driving signal should be lower than ~780 Hz, judging from the frequency response shown in Fig. 2(a). For scanning at 85 Hz, the highest harmonics should be less than the ninth order (i.e., 745 Hz). Figure 2(g) shows a rounded triangular wave constructed from harmonics up to the ninth order (black line) and the corresponding displacement of the X-scanner (red line). The displacement did not show noticeable vibrations. The nonlinear scan range is about 10% of the full scan range, which is much smaller than that when a sinusoidal scan wave is used.

For actual imaging, we combined these two damping methods (as well as compensating for the nonlinearity and interference of the X- and Y-scanners' displacements, as described later); the rounded triangular wave containing higher harmonics up to the ninth order was filtered through an inversed transfer function constructed using the measured frequency response. By using this combination, the fundamental frequency of X-scanning could be extended up to ~1 kHz, as shown in Fig. 2(h).

For Y-scanning, a sawtooth wave is typically used. The quick return to the scan origin along the Y-direction, which is performed after the completion of line scans in the X-direction, easily generates vibrations. We avoided vibration generation by slowing the return scan. Even when the return scan to the origin is slowed, the time it takes is much shorter than the time for which an image is captured.

B. Compensation for nonlinearity

All piezoelectric actuators have an intrinsic hysteresis that distorts the AFM image owing to their nonlinear displacement as a function of the applied voltage. The position error generally becomes 10%–15% of the full scan range,[29] which causes considerable image distortion, especially for wide-area imaging. Two types of control methods have been proposed to compensate for the nonlinear hysteresis curve: closed-loop[30] and open-loop[31] compensations. The former enables more precise control than the latter. However, the use of closed-loop compensation makes the scanner assembly complicated because of the implementation of displacement sensors. Moreover, the bandwidth of high-precision displacement sensors is too low for application to high-speed scanners. In the open-loop method, the nonlinearity is compensated for by the use of a feed-forward inverse model. Here, we used open-loop compensation based on the pre-measured nonlinear hysteresis curves.

Figure 3(a) shows hysteresis curves of the X-scanner for displacement ranges of 40 μm (red line) and 24 μm (blue line). Figure 3(d) shows the effect of hysteresis on an AFM image of a square grating with a pitch of 10 μm. The image was acquired without compensation at 15 s/frame for a 33 × 33 μm^2 area. The image shows grating pitches with variations of approximately ±20% and ±15% in the X- and

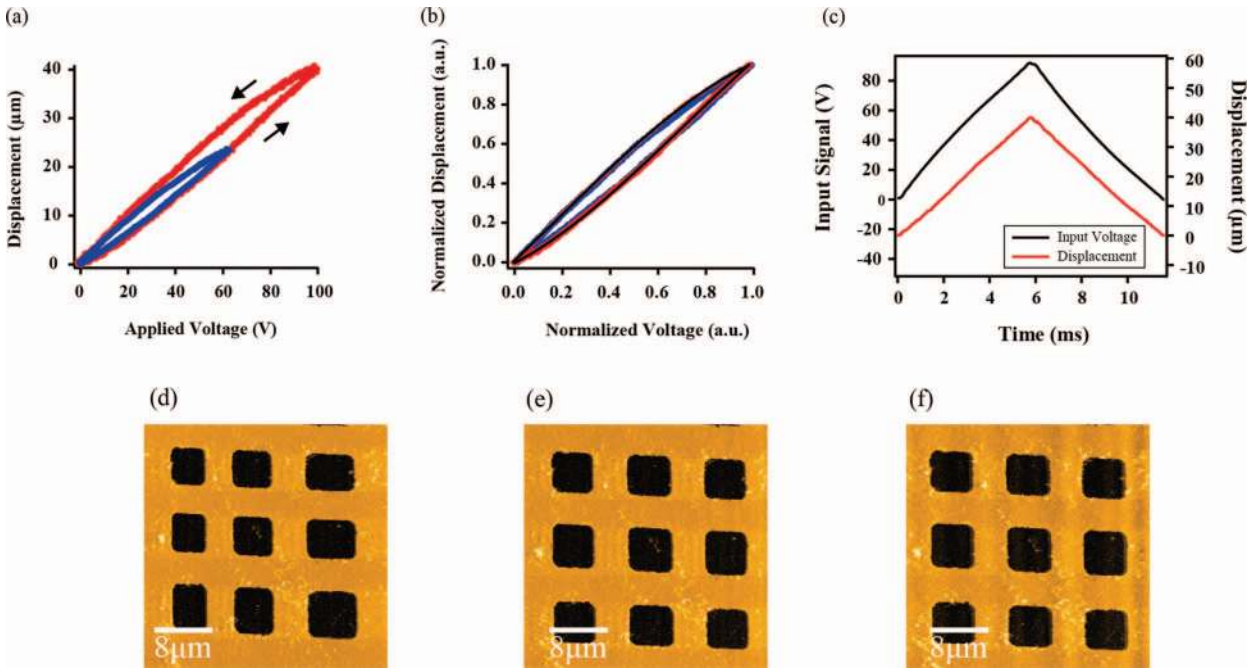

FIG. 3. Hysteresis of X-scanner and its compensation. (a) Hysteresis curves for two different ranges (blue line, 24 μm; red line, 40 μm). (b) Hysteresis curves normalized with regard to both displacement and voltage. Black line shows a fitting curve with fourth-order polynomials. (c) Driving signal of 85 Hz with a triangular wave form modified by open-loop compensation for hysteresis (black line) and corresponding displacement (red line). Here, hysteresis compensation was applied to a triangular wave form modified by inverse compensation. (d) AFM image of a test grating sample with a pitch of 10 μm obtained without hysteresis compensation (imaging rate, 7 s/frame; pixels, 256 × 256). (e) AFM image of the same grating sample obtained using hysteresis compensation (imaging rate, 7 s/frame; pixels, 256 × 256). (f) AFM image of the same grating sample obtained using hysteresis compensation (imaging rate, 3 s/frame; pixels, 256 × 256).

Y-directions, respectively. Figure 3(b) shows hysteresis curves that are the same as those shown in Fig. 3(a) but normalized with respect to both the displacement and the applied voltage. The normalized curves are identical irrespective of the displacement ranges, meaning that the nonlinearity of the piezoactuator is independent of the scan range. We confirmed that the normalized curves obtained for other scan ranges are also identical. The normalized expansion and contraction curves can be fitted by fourth-order polynomial functions, as shown by the black lines in Fig. 3(b). Although higher-order polynomial functions give better fitting, the fourth-order fitting is good enough practically to compensate for the hysteresis. The driving voltage signal that was not processed for inverse vibration damping but compensated for the hysteresis was first constructed using the inverse functions of the fitted hysteresis curves. Then, this driving signal was processed for inverse vibration damping or for both inverse vibration damping and rounding the vertices of the signal. Figure 3(c) shows the effect of hysteresis compensation on the displacement of the X-scanner. The black line indicates a driving signal of 85 Hz constructed by this method (here, the process of rounding vertices is omitted), and the red line indicates the corresponding displacement of the X-scanner. The outwardly (ascending regime) and inwardly (descending regime) distorted curves of the driving signal reflect the compensation for hysteresis. It is apparent that the X-scanner is displaced linearly in both the expansion and contraction regimes. As a result, the distortion of the grating image was much improved, as shown by the image in Fig. 3(e) captured at 7 s/frame. The variations in the grating pitch are now less than ±1%. As shown in Fig. 3(f), even when an image is captured at 3 s/frame, the image distortion is eliminated, except for the rhombic distortion of the square grid holes, which is due to interference between the X- and Y-scanners.

C. Compensation for interference between X- and Y-scanners

Interference between the X- and Y-scanners occurs because the free ends of the levers used for displacement magnification do not move in a straight line. The green and red lines in Fig. 4(a) show the sample stage displacement in the Y-direction as a function of the X-scanner displacement (driving voltage was applied only to the X-piezoactuator) up to 5 μm (green line) and 30 μm (red line). The sample stage moved almost linearly in the Y-direction with a coupling ratio of 0.017 (i.e., 17 nm per 1 μm displacement of the X-scanner). Note that the two methods of active damping and the compensation for the hysteresis effect were applied in this experiment as well as in the following experiments in this subsection. To eliminate this interference, an appropriate fraction of the voltage applied to the X-piezoactuator was subtracted from the driving signal for the Y-piezoactuator. As shown by the black and yellow lines in Fig. 4(a), this method minimized the coupled movement of the sample stage in the Y-direction, irrespective of the displacement range of the X-scanner. The sample stage was also passively moved in the X-direction when the Y-scanner was displaced, as shown by the green and red lines in Fig. 4(b). This interference was also minimized by

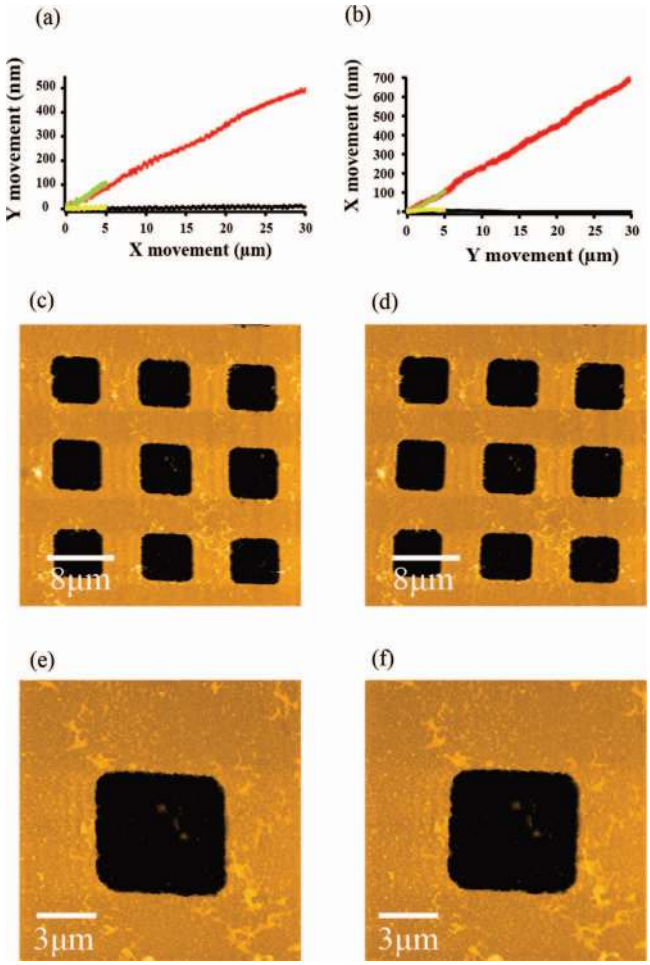

FIG. 4. Elimination of interference between X- and Y-scanner displacements. (a) Sample stage displacement in the Y-direction as a function of X-scanner displacement. Displacement ranges of X-scanner are 5 μm (green line) and 30 μm (red line). Yellow and black lines represent displacements in the Y direction when interference compensation was applied for X-scanner displacements of 5 μm and 30 μm, respectively. (b) Sample stage displacement in the X-direction as a function of Y-scanner displacement. Displacement ranges of Y-scanner are 5 μm (green line) and 30 μm (red line). Yellow and black lines represent displacements in the X direction when interference compensation was applied for Y-scanner displacements of 5 μm and 30 μm, respectively. (c) AFM image of a test grating sample with a pitch of 10 μm obtained without interference compensation (scan range, 33 × 33 μm^2; imaging rate, 7 s/frame; pixels, 256 × 256). The square grids are distorted in a rhombic shape. (d) AFM image of the same sample obtained using interference compensation (imaging rate, 7 s/frame; pixels, 256 × 256). (e) Enlarged AFM image of the sample obtained without interference compensation (scan range, 15 × 15 μm^2; imaging rate, 7 s/frame; pixels, 256 × 256). (f) Enlarged AFM image of the sample obtained using interference compensation (scan range, 15 × 15 μm^2; imaging rate, 7 s/frame; pixels, 256 × 256).

the same method, as shown by the yellow and black lines in Fig. 4(b). As a result, the images of square grid holes with rhombic distortion shown in Figs. 4(c) [imaged under the condition identical to that used for Fig. 3(e)] and 4(e) were converted to images with much less distortion, as shown in Figs. 4(d) and 4(f), respectively.

D. Z-scanner

The feedback bandwidth is one of the most important factors in achieving fast imaging of soft biological samples

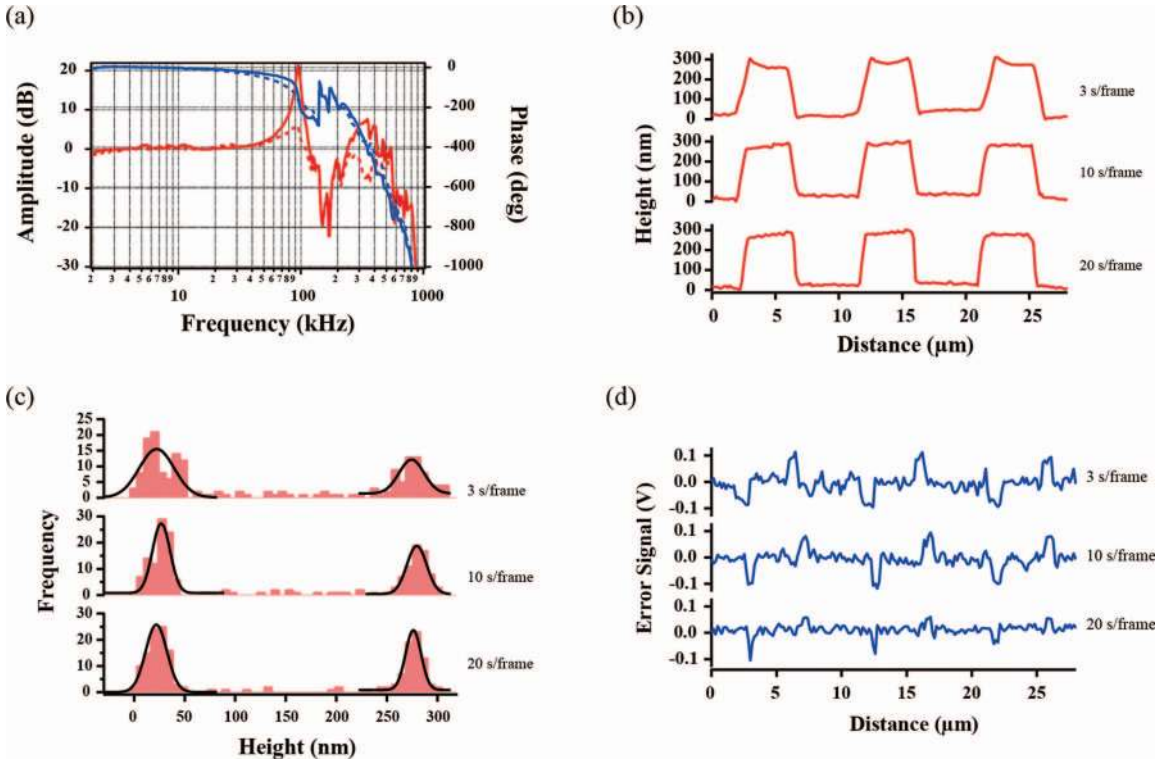

FIG. 5. Tracing accuracy of feedback Z-scanning by the wide-area scanner. (a) Frequency response of the Z-scanner (gain, red lines; phase, blue lines) obtained with (dotted lines) and without (solid lines) the use of active Q-control damping. (b) Cross sections of topographic AFM images (256 × 256 pixels) of a grating sample acquired at different imaging rates (top, 3 s/frame; middle, 10 s/frame; bottom, 20 s/frame). (c) Histograms of topographic height measured for the top surface of the grating sample. The average heights measured are 276 nm (top, 3 s/frame), 279 nm (middle, 10 s/frame), and 276 nm (bottom, 20 s/frame). (d) Cross sections of the error-signal images that appeared when the grating sample was imaged at different imaging rates.

because delayed movement of the Z-scanner increases the loading force from the AFM tip to the sample. The feedback bandwidth depends on several delay factors such as the mechanical properties of the *Z*-piezoactuator and the cantilever and imaging conditions.[32,33] Among the delay factors, the response delay of the *Z*-piezoactuator is the major one because the resonant frequency of the Z-piezoactuator suitable for observing a large specimen is much lower than that of small cantilevers optimized for HS-AFM. For the Z-scanner, we used a stack piezoactuator with dimensions of $2 \times 3 \times 5$ mm^3 (AE0203D04F, Tokin-NEC) having a maximum displacement of 2.5 μm at 100 V, which was glued to the top of the supporting base to be moved in the X- and Y-directions. As a counterweight, the same type of piezoactuator was also glued to the bottom side of the supporting base. This additional piezoactuator is displaced so that the impulsive force exerted on the supporting base by the rapid displacement of the Z-scanner is counteracted.[32] Figure 5(a) shows the frequency response of the Z-scanner. Here, the displacement was measured at the cylindrical glass stage (1.5 mm diameter) attached to the Z-scanner. The first 90 kHz and higher-frequency peaks were damped by using the active Q-control technique,[34] as shown by the dotted red (amplitude) and blue (phase) lines in Fig. 5(a). The peak gain at the first resonant frequency was damped to about 3 dB. Although further damping was possible, we attenuated damping to this extent to minimize the phase delay at lower frequencies.

In the following imaging experiments in this subsection, the two methods of active damping as well as the compensation for nonlinearity and interference mentioned above were applied. Figures 5(b) and 5(d) show cross sections along the X-scan direction of the topographic and error-signal images obtained for a square grating (pitch, 10 μm), respectively. The 256 × 256 pixel images were acquired at rates of 3 s/frame (top), 10 s/frame (middle), and 20 s/frame (bottom), which correspond to scan velocities of 6.8 mm/s, 2.0 mm/s, and 1 mm/s, respectively. Dynamic proportional-integral-derivative (PID) control was used to reduce the parachuting time during which the cantilever tip was completely detached from the sample surface at its bottom swing;[35] the gain parameters of the PID controller were automatically altered depending on the cantilever's oscillation amplitude. From the histograms of the topographic heights shown in Fig. 5(c), the heights are almost the same irrespective of the imaging rate: 276 nm (top, 3 s/frame), 279 nm (middle, 10 s/frame), and 276 nm (bottom, 20 s/frame), although the height variation becomes larger at faster imaging rates. This consistency demonstrates that the feedback Z-scan is able to track the surface because variations in the error signals appear only around the grating edges, whereas the error signal is mostly constant over 80% of the flat areas even at the fastest imaging rate [Fig. 5(d)].

The maximum displacement of the Z-piezoactuator used here is limited to 2.5 μm. We may need a larger displacement depending on the sample to be observed. We can

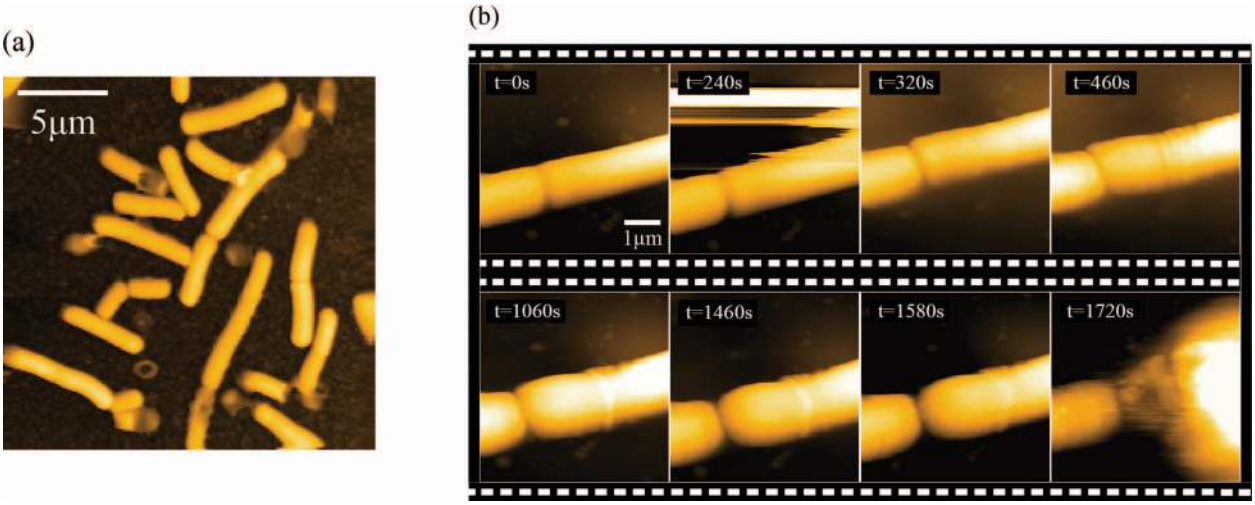

FIG. 6. HS-AFM imaging of *B. subtilis* using the wide-area scanner. (a) Topographic image of *B. subtilis* in a culture medium solution before the addition of lysozyme. Scan range, 20 × 20 μm^2; imaging rate, 15 s/frame; pixels, 200 × 200. (b) Successive images of bacteriolysis process of *B. subtilis* subjected to lysozyme. Lysozyme was injected at $t = 240$ s. Scan range, 5 × 5 μm^2; imaging rate, 20 s/frame; pixels, 256 × 256 (enhanced online). [URL: http://dx.doi.org/10.1063/1.4803449.1]

alternatively use a longer piezoactuator with dimensions of 2 × 3 × 10 mm^3 (AE0203D16F, Tokin-NEC), which can be displaced up to 4.3 μm at 100 V. However, we have to sacrifice the imaging rate because the resonant frequency of the longer piezoactuator is lowered to approximately a half (50 kHz). When this piezoactuator was used, the maximum possible imaging rate was reduced to ∼7 s/frame for 256 × 256 pixel imaging of the same grating sample.

IV. IMAGING OF BIOLOGICAL SAMPLES

To demonstrate the capability of the wide-area scanner, we imaged live bacterial and eukaryotic cells using the scanner under control by all the techniques mentioned above.

A. Large-area imaging

1. Imaging of Bacillus subtilis

We first observed the process of bacteriolysis of a rod-shaped *B. subtilis* (approximately 700 nm in diameter and 2 μm long) subjected to lysozyme. *B. subtilis* has been widely used as a model system for investigating the roles of autolysins in the cell wall metabolism of endospore-forming Gram-positive bacteria, and the structure of peptidoglycan and spores[36–38] because of its nonpathogenicity and amenability to genetic manipulation. It is well-known that *B. subtilis* is susceptible to the antibacterial action of lysozyme, which hydrolyzes 1,4-beta linkages between *N*-acetyl glucosamine and *N*-acetyl muramic acid, leading to degradation of peptidoglycan in the cell wall.[37] Here, we captured this degradation process to demonstrate the capability of the wide-area HS-AFM scanner.

The bacterial cells were immobilized on a glass stage coated with poly-L-lysine (0.1 mg/ml). HS-AFM imaging was conducted in a culture medium (Penassay Broth). Figure 6(a) shows a wide-area image of the cells captured over an area of 20 × 20 μm^2 at 15 s/frame (200 × 200 pixels). The mean height of the cells was 730 nm, indicating accurate tracing of the cell topography. Figure 6(b) (see video) shows some of the images of the bacterium before and after the addition of lysozyme, successively captured at 20 s/frame (256 × 256 pixels). Before the injection of lysozyme ($t = 0$ s), the cell surface appears smooth. At $t = 240$ s, lysozyme (final concentration, 80 μM) was injected into the observation solution, and therefore, the imaging was somewhat disturbed. Then, after $t = 320$ s, the surface morphology gradually became varied, and wrinkle structures perpendicular to the long cell axis appeared. At the same time, the cell gradually swelled ($t = 1060$ s, 1460 s, and 1580 s). Finally, at $t = 1720$ s, the cell exploded, probably because of excessive osmotic pressure from inside of it, resulting in partial exposure of the intracellular contents. We also observed the morphological changes induced by lysozyme (final concentration, 200 μM) at a faster imaging rate, 2 s/frame, for 120 × 90 pixels (Fig. 7). The cell surface roughness increased rapidly with a time lag of ∼90 s after the injection of lysozyme at $t = 32$ s, as shown in Fig. 7(a). The corresponding images are shown in Fig. 7(b) (see video). Here, the surface roughness was expressed by the root-mean-square roughness of the area indicated by the white rectangle in Fig. 7(b). The roughness was almost constant (∼93 nm) before the injection of lysozyme, whereas it increased to ∼125 nm after the injection. The increase in the roughness was well fitted by a single exponential function with a time constant of $\tau = 36.8$ s, as indicated by the solid line in Fig. 7(a).

2. Imaging of HeLa cells

We tested whether large-area imaging could be conducted even for live eukaryotic cells, which are much softer than bacteria. HeLa cells, one of the most commonly used immortal cell lines derived from human cancer cells, were maintained on a poly-L-lysine-coated glass stage at 37 °C in 5% CO_2 using Dulbecco's modified Eagle's medium (Life Technologies) supplemented with 10% fetal bovine serum (Life Technologies). HS-AFM imaging was performed in

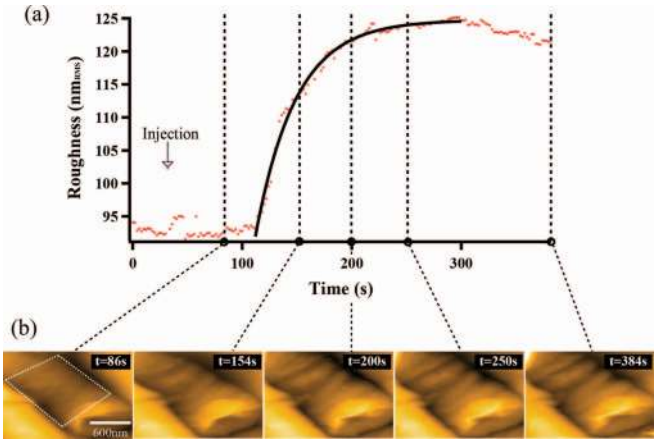

FIG. 7. Time course of roughness change of the outer surface of *B. subtilis* subjected to lysozyme. (a) Time course of root mean square (RMS) roughness. Lysozyme was injected at $t = 32$ s. Solid line shows the result of best fitting (time constant, $\tau = 36.8$ s) by a single exponential function for the time course between $t = 112$ s and $t = 300$ s. (b) Corresponding AFM images of the outer surface of *B. subtilis* at different time lapses. Values of RMS roughness were calculated for the area encircled by the white broken line shown in the image at $t = 86$ s (enhanced online). [URL: http://dx.doi.org/10.1063/1.4803449.2]

HEPES-buffered artificial cerebrospinal fluid (H-ACSF) at 32 °C. The fine structures of HeLa cells were successfully imaged by HS-AFM at 5 s/frame (200 × 200 pixels). Sheet-like structures with ~100 nm height were observed at the cell edge regions. Interestingly, the HS-AFM movie clearly showed a continuous flow of small objects directed from the cell periphery toward the center of the cell body, as shown in Fig. 8(a) (see video).

It is well known that actin filaments polymerize at the leading edge of eukaryotic cells and flow back into the cell body in the so-called actin retrograde flow.[39,40] To determine the origin of the flow observed by HS-AFM and its relationship to the actin retrograde flow, cytochalasin D (Sigma), a chemical inhibitor of actin polymerization, was bath-applied to HeLa cells. A HS-AFM movie showed that the continuous flow stopped completely after the application of cytochalasin D (final concentration: 20 ng/ml) [Fig. 8(b)] (see video), indicating that the flow observed in the HS-AFM movies is the actin retrograde flow.

Next, we conducted real-time observations of endocytosis by HS-AFM. Endocytosis is a cellular process in which cells bring molecules or substances into the cell interior from the outside of the cell by engulfing them with the cell membrane. The engulfment typically begins with the formation of nanoscale pits on the cell surface. The small GTPase Rab5 is known to be crucial in regulation of endocytosis. Its constitutive active mutant Rab5(Q79L) stimulates endocytosis,[41–43] and replacement of the C-terminus of Rab5 with CAAX box derived from k-Ras enhances the plasma membrane localization of Rab5. Figure 8(c) shows successive AFM images of a HeLa cell in which mEGFP-Rab5(Q79L)-CAAX is overexpressed. Here, mEGFP was co-expressed with Rab5(Q79L) and Rab5(Q79L)-CAAX in the HeLa cells to evaluate the overexpression level by fluorescence microscopy. As seen in Fig. 8(c) (see video), each of the two pits encircled by broken lines was capped by a membrane protrusion that grew with time from the membrane surrounding each pit (5 s/frame, 200 × 200 pixels). This process resembles the recent observation of endocytosis-mediated pit closure on the

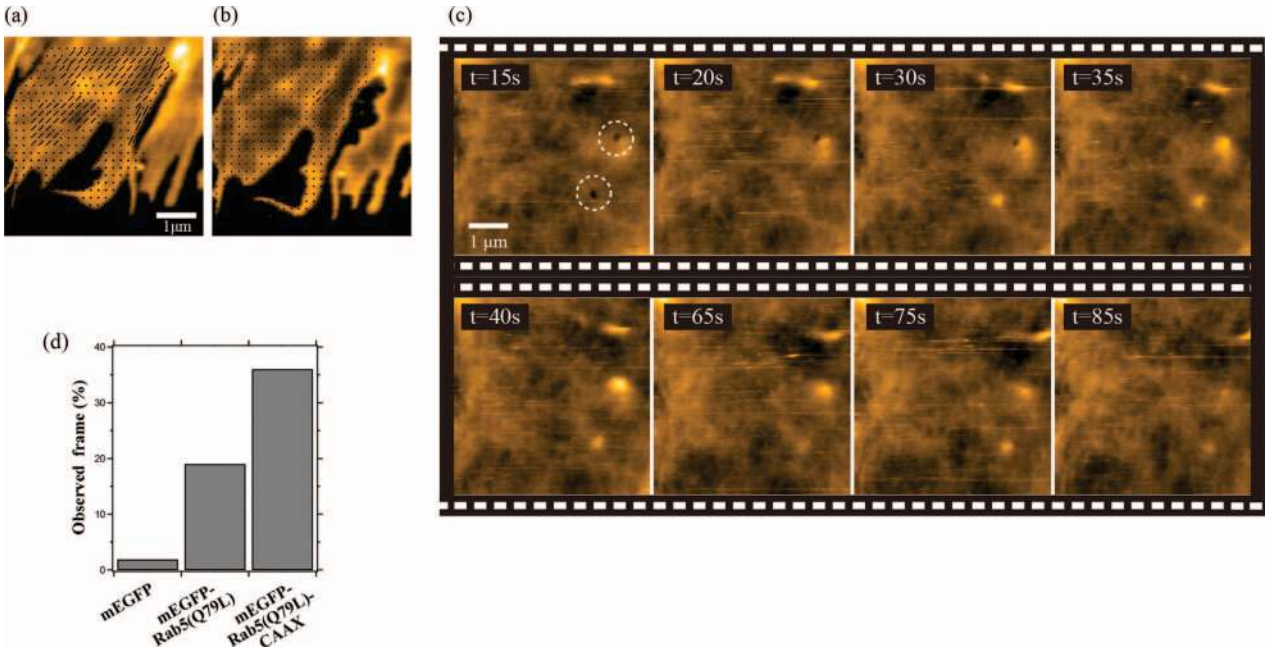

FIG. 8. HS-AFM imaging of dynamic processes occurring in HeLa cells. (a) Topographic image of HeLa cell at an edge region before the addition of cytocharasin D. Thin black lines indicate flow of small objects. Imaging rate, 5 s/frame; pixels, 200 × 200. (b) Topographic image of HeLa cell at an edge region after the addition of cytocharasin D. Black dots show that no flow is occurring. Scan range, 5 × 5 μm^2; imaging rate, 5 s/frame; pixels, 200 × 200. (c) Successive images showing the dynamic process of endocytosis. HeLa cells were transfected by mEGFP-Rab5(Q79L)-CAAX. The imaging was performed 24 h after transfection. Scan range, 5 × 5 μm^2; imaging rate, 5 s/frame; pixels, 200 × 200. (d) Frequencies of pit appearance in HeLa cells transfected by mEGFP, mEGFP-Rab5(Q79L), and mEGFP-Rab5(Q79L)-CAAX (enhanced online). [URL: http://dx.doi.org/10.1063/1.4803449.3] [URL: http://dx.doi.org/10.1063/1.4803449.4] [URL: http://dx.doi.org/10.1063/1.4803449.5]

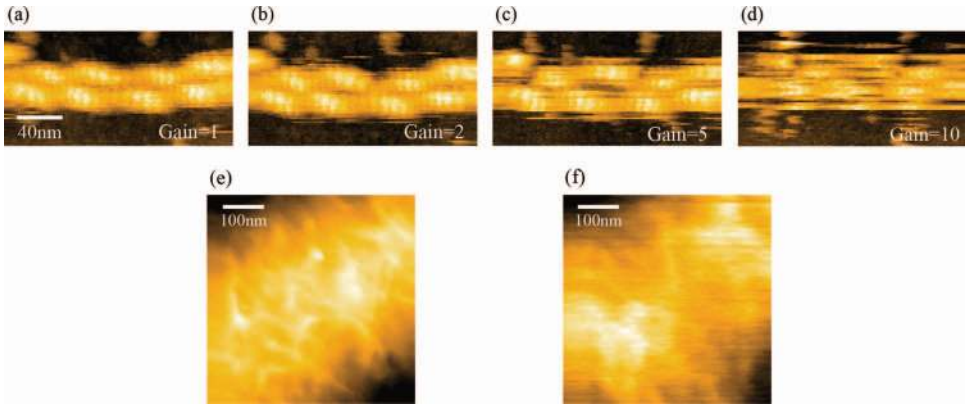

FIG. 9. Narrow-area imaging by HS-AFM equipped with the wide-area scanner and effect of the gain-variable piezodriver on imaging. (a)–(d) HS-AFM images of two actin filaments aligned in parallel obtained with different piezodriver gains [(a) ×1; (b) ×2; (c) ×5; (d) ×10]. Scan range, 200 × 100 nm^2; imaging rate, 0.15 s/frame; pixels, 120 × 60. (e) and (f) AFM images of outer surface of *B. subtilis* before (e) and after (f) injection of lysozyme. Scan range, 500 × 500 nm^2; imaging rate, 2 s/frame; pixels, 256 × 256.

surface of COS-7 cells revealed by scanning ion conductance microscopy.[44] Figure 8(d) shows histograms of the observed rates of pit formation for three types of cells in each of which mEGFP, mEGFP-Rab5(Q79L), or mEGFP-Rab5(Q79L)-CAAX is overexpressed. The nanoscale pits were infrequently observed in HeLa cells transfected only by mEGFP (1.9% of a total of 2689 frames of 27 cells), whereas the frequency of nanoscale pit appearance was significantly increased by overexpression of mEGFP-Rab5(Q79L) (19% of a total of 3994 frames of 30 cells) and further increased by overexpression of mEGFP-Rab5(Q79L)-CAAX (36% of a total of 3090 frames of 24 cells), consistent with a persistent stimulation effect of Rab5 mutants on endocytosis.[41–43] Thus, we demonstrated here that wide-area HS-AFM can also be used to visualize dynamic processes occurring in very soft eukaryotic cells.

B. Small-area imaging

The large-area imaging capability achieved here allows us to easily position the AFM tip on a specific area of interest within a pre-imaged large object. If the wide-area scanner has a high-resolution imaging capability even when it is used to image a small area, it becomes possible to image dynamic events involving tiny objects such as molecules in narrow areas within a pre-imaged large object. To achieve this capability, we have to improve the resolution of the wide-area scanner without reducing the wide-area positioning capability. The extension coefficient of the X- and Y-piezoactuators used for the wide-area scanner is large (435 nm/V). To effectively use this large coefficient, the gain of the piezodriver should be high (we used a ×10 gain). However, the fast digital-to-analog convertor has a limited resolution (12 bits for a 10 V range in our case). Consequently, the lateral resolution is limited to approximately 11 nm. To solve this problem while maintaining the wide-area positioning capability, we developed a new piezodriver with two-channel inputs (now commercially available: M-2345, MESS-TEC Co.). The first channel with selectable gains (×1, ×2, ×5, and ×10) is used for scanning (hence, for imaging), whereas the second channel with a fixed gain (×10) is used for positioning. The gains of the first channel are selected depending on the size of the area to be imaged.

We tested this piezodriver's capacity for high-resolution imaging by imaging actin filaments anchored on a mica surface [Figs. 9(a)–9(d)]. The HS-AFM images in Figs. 9(a)–9(d) were obtained with driver gains of ×1, ×2, ×5, and ×10, respectively, whereas the scan area and imaging rate are fixed at 200 × 100 nm^2 (120 × 60 pixels) and 0.15 s/frame, respectively. As seen in Figs. 9(a) and 9(b), not only the helical structure with a 36-nm pitch but also actin monomers within the filaments are resolved. On the other hand, when the driver gain was increased to ×5 and ×10, the image quality deteriorated significantly because of lower bit resolutions.

Figure 9(e) shows a high-resolution image of the cell surface of *B. subtilis* not subjected to lysozyme. The image was obtained at a piezodriver gain of ×1 and an imaging rate of 2 s/frame for a scan area of 500 × 500 nm^2 (200 × 200 pixels). Fine structures on the cell wall were clearly visible, whereas they could not be resolved by large-area imaging, as shown in Fig. 6(b) (t = 0 s). Soon after the injection of lysozyme, the fine structure on the cell surface became blurry owing to degradation of the cell wall, and a wrinkle structure with a periodicity of about 300 nm appeared, as shown in Fig. 9(f).

V. CONCLUSIONS

We developed techniques to achieve both fast and wide-area scanning capabilities. The wide-area scanner developed can be scanned over ∼46 × 46 μm^2. Unwanted vibrations produced during rapid scanning were eliminated by inverse compensation combined with the use of rounded vertices on a triangular scan wave constructed with a limited number of Fourier components. The nonlinear displacement arising from the hysteresis of the piezoactuators and interference between the X- and Y-scanners was also eliminated. As a result, a test grating sample was imaged at 3 s/frame for a scan area of 40 × 40 μm^2. Finally, the fast scan capability of the wide-area scanner was demonstrated by imaging of dynamic processes including lysozyme-induced bacteriolysis, actin retrograde flow, and endocytosis. It was also demonstrated

that the wide-area scanner retains its capacity for high-speed, high-resolution imaging even when used for a small imaging area. Thus, the range of samples to which HS-AFM can be applied is now greatly extended, from single molecules to live cells.

ACKNOWLEDGMENTS

This work was supported by the Human Frontier Science Program, a Grant-in-Aid for Basic Research (Project ID: 24227005, 23115008), the Knowledge Cluster Initiative Project funded by the Ministry of Education, Culture, Sports, Science and Technology in Japan, JST/ALCA, and by a program on Development of Systems and Technology for Advanced Measurement and Analysis funded by JST.

[1]M. B. Viani, L. I. Pietrasanta, J. B. Thompson, A. Chand, I. C. Gebeshuber, J. H. Kindt, M. Richter, H. G. Hansma, and P. K. Hansma, Nat. Struct. Biol. **7**, 644 (2000).
[2]T. Ando, N. Kodera, E. Takai, D. Maruyama, K. Saito, and A. Toda, Proc. Natl. Acad. Sci. U.S.A. **98**, 12468 (2001).
[3]A. D. L. Humphris, M. J. Miles, and J. K. Hobbs, Appl. Phys. Lett. **86**, 034106 (2005).
[4]T. Ando, Nanotechnology **23**, 062001 (2012).
[5]Y. Shinozaki, K. Sumitomo, M. Tsuda, S. Koizumi, K. Inoue, and K. Torimitsu, PLoS Biol. **7**, e103 (2009).
[6]N. Kodera, D. Yamamoto, R. Ishikawa, and T. Ando, Nature (London) **468**, 72 (2010).
[7]M. Shibata, H. Yamashita, T. Uchihashi, H. Kandori, and T. Ando, Nat. Nanotechnol. **5**, 208 (2010).
[8]M. Shibata, T. Uchihashi, H. Yamashita, H. Kandori, and T. Ando, Angew. Chem., Int. Ed. **50**, 4410 (2011).
[9]T. Uchihashi, R. Iino, T. Ando, and H. Noji, Science **333**, 755 (2011).
[10]S. F. J. Wickham, M. Endo, Y. Katsuda, K. Hidaka, J. Bath, H. Sugiyama, and A. J. Turberfield, Nat. Nanotechnol. **6**, 166 (2011).
[11]D. Yamamoto, N. Nagura, S. Omote, M. Taniguchi, and T. Ando, Biophys. J. **97**, 2358 (2009).
[12]I. Casuso, P. Sens, F. Rico, and S. Scheuring, Biophys. J. **99**, L47 (2010).
[13]K. Igarashi, T. Uchihashi, A. Koivula, M. Wada, S. Kimura, T. Okamoto, M. Penttilä, T. Ando, and M. Samejima, Science **333**, 1279 (2011).
[14]D. Yamamoto, T. Uchihashi, N. Kodera, and T. Ando, Nanotechnology **19**, 384009 (2008).
[15]H. Yamashita, K. Voïtchovsky, T. Uchihashi, S. A. Contera, J. F. Ryan, and T. Ando, J. Struct. Biol. **167**, 153 (2009).
[16]A. Miyagi, Y. Tsunaka, T. Uchihashi, K. Mayanagi, S. Hirose, K. Morikawa, and T. Ando, Chem. Phys. Chem. **9**, 1859 (2008).
[17]G. Schitter and A. Stemmer, IEEE Trans. Control Syst. Technol. **12**, 449 (2004).
[18]I. Choi, Y. Kim, J. H. Kim, Y. I. Yang, J. Lee, S. Lee, S. Hong, and J. Yi, Nanotechnology **19**, 445701 (2008).
[19]A. J. Fleming, B. J. Kenton, and K. K. Leang, Ultramicroscopy **110**, 1205 (2010).
[20]G. E. Fantner, R. J. Barbero, D. S. Gray, and A. M. Belcher, Nat. Nanotechnol. **5**, 280 (2010).
[21]G. Schitter, K. J. Åström, B. E. DeMartini, P. J. Thurner, K. L. Turner, and P. K. Hansma, IEEE Trans. Control Syst. Technol. **15**, 906 (2007).
[22]J. H. Kindt, G. E. Fantner, J. A. Cutroni, and P. K. Hansma, Ultramicroscopy **100**, 259–265 (2004).
[23]I. A. Mahmood and S. O. R. Moheimani, Nanotechnology **20**, 365503 (2009).
[24]Y. K. Yong, S. O. R. Moheimani, and I. R. Petersen, Nanotechnology **21**, 365503 (2010).
[25]A. Bazaei, Y. K. Yong, and S. O. R. Moheimani, Rev. Sci. Instrum. **83**, 063701 (2012).
[26]Y. Li and J. Bechhoefer, Rev. Sci. Instrum. **78**, 013702 (2007).
[27]A. J. Fleming and A. G. Wills, in *Proceedings of the IFAC World Congress, Seoul, Korea, 7–11 July* (Elsevier, Netherlands, 2008), p. 11805.
[28]K. K. Leang and A. J. Fleming, Asian J. Control **11**, 144 (2009).
[29]P. Ge and M. Jouaneh, IEEE Trans. Control Syst. Technol. **4**, 209 (1996).
[30]S. K. Hung, E. T. Hwu, I. S. Hwang, and L. C. Fu, Jpn. J. Appl. Phys. **45**, 1917 (2006).
[31]B. Mokaberi and A. A. G. Requicha, IEEE Trans. Autom. Sci. Eng. **5**, 197 (2008).
[32]T. Ando, T. Uchihashi, and T. Fukuma, Prog. Surf. Sci. **83**, 337 (2008).
[33]T. Ando, T. Uchihashi, and N. Kodera, Jpn. J. Appl. Phys. **51**, 08KA02 (2012).
[34]N. Kodera, H. Yamashita, and T. Ando, Rev. Sci. Instrum. **76**, 053708 (2005).
[35]N. Kodera, M. Sakashita, and T. Ando, Rev. Sci. Instrum. **77**, 083704 (2006).
[36]A. Ryter and O. E. Landman, J. Bacteriol. **88**, 457 (1964).
[37]J. Ghuysen, Bacteriol. Rev. **32**, 425 (1968).
[38]T. J. Smith, S. A. Blackman, and S. J. Foster, Microbiology **146**, 249 (2000).
[39]T. Mitchison and M. Kirschner, Neuron **1**, 761 (1988).
[40]P. Forscher and S. J. Smith, J. Cell Biol. **107**, 1505 (1988).
[41]J. P. Gorvel, P. Chavier, M. Zerial, and J. Gruenberg, Cell **64**, 915 (1991).
[42]M. A. Barbieri, G. Li, M. I. Colombo, and P. D. Stahl, J. Biol. Chem. **269**, 18720–18722 (1994).
[43]C. Bucci, R. G. Parton, I. H. Mather, H. Stunnenberg, K. Simons, B. Hoflack, and M. Zerial, Cell **70**, 715–728 (1992).
[44]A. I. Shevchuk, P. Novak, M. Taylor, I. A. Diakonov, A. Ziyadeh-Isleem, M. Bitoun, P. Guicheney, M. J. Lab, J. Gorelik, C. J. Merrifield, D. Klenerman, and Y. E. Korchev, J. Cell. Biol. **197**, 499–508 (2012).